J Low Temp Phys
DOI 10.1007/s10909-016-1666-x

Calorimetric Observation of Single He_2^* Excimers in a 100-mK He Bath

F. W. Carter[1,2,3] · S. A. Hertel[3,4,5] · M. J. Rooks[6] · P. V. E. McClintock[7] · D. N. McKinsey[3,4,5] · D. E. Prober[8]

Received: 24 July 2016 / Accepted: 27 September 2016

Abstract We report the first calorimetric detection of individual He_2^* excimers within a bath of superfluid ^{4}He. The detector used in this work is a single superconducting titanium transition edge sensor (TES) with an energy resolution of ∼1 eV, immersed directly in the helium bath. He_2^* excimers are produced in the surrounding bath using an external gamma-ray source. These excimers exist either as short-lived singlet or long-lived triplet states. We demonstrate detection (and discrimination) of both states: In the singlet case the calorimeter records the absorption of a prompt ≈15 eV photon, and in the triplet case the calorimeter records a direct interaction of the molecule with the TES surface, which deposits a distinct fraction of the ≈15 eV, released upon decay, into the surface. We also briefly discuss the detector fabrication and characterization.

Keywords Helium excimer detection · Superconducting detector · Transition edge sensor · Superfluid helium

✉ F. W. Carter
faustin.carter@gmail.com

1 Argonne National Laboratory, High Energy Physics, Lemont, IL 60439, USA
2 Kavli Institute for Cosmological Physics, Chicago, IL 60637, USA
3 Department of Physics, Yale University, New Haven, CT 06511, USA
4 Department of Physics, University of California, Berkeley, Berkeley, CA 94720, USA
5 Lawrence Berkeley National Laboratory, Berkeley, CA 94720, USA
6 Yale Institute for Nanoscience and Quantum Engineering, New Haven, CT 06520, USA
7 Department of Physics, Lancaster University, Lancaster LA1 4YB, UK
8 Department of Applied Physics, Yale University, New Haven, CT 06511, USA

Published online: 11 October 2016

1 Introduction

Superfluid helium, when subjected to ionizing radiation, produces metastable diatomic He molecules in both the singlet and triplet states, emitting a ≈15 eV photon upon decay. The singlet $He_2^*(A^1\Sigma_u^+)$ decays within nanoseconds, while the triplet $He_2^*(a^3\Sigma_u^+)$ exhibits a remarkably long lifetime of 13 s in superfluid helium [1]. The long-lived triplet state can serve as an observable tracer particle in a liquid helium bath, tagging the flow of the normal-fluid component or, at colder temperatures, tagging quantized vortices in the superfluid component [2]. Efficient detection of helium excimers may also enable the use of a superfluid helium bath in a search for dark matter-induced nuclear recoils, given that a recoil's resulting singlet/triplet excimer ratio distinguishes between electron- and nuclear recoils. Additionally, high-sensitivity detection of electronic excitations may be used to veto electron recoil backgrounds when searching for low-energy nuclear recoils, since nuclear recoils predominantly produce heat in the form of rotons and phonons [3].

These applications require an efficient technique for observing and differentiating between the two excimer states. Two techniques have been employed previously for triplet excimer detection: observation through laser fluorescence [4,5] and observation of Auger electrons produced through quenching on a surface [6,7]. Low-temperature calorimetry offers near-unity efficiency for detecting *any* energy deposition above some energy threshold, making both the ≈15 eV singlet decay photons and the triplet surface quench process observable with the same sensor. Here we report success at this high-efficiency detection of both excimer states by a single sensor.

In this work, we employ a single transition edge sensor (TES) with resolution of ∼1 eV at 15 eV, similar to a prototype discussed in earlier work [8]. The detector is immersed directly in a superfluid helium bath at 100 mK (the Kapitza resistance between the sensor and liquid helium allows the sensor to function even while in contact with the superfluid helium), and excimers are created by exposing the bath to gamma rays from a 100 − μCurie ^{22}Na source located outside the cryostat. The superfluid reservoir, the cryostat, and the electronics are described in Carter [9].

2 The Transition Edge Sensor

The TES consists of a 15-nm film of evaporated titanium with 300-nm thick evaporated aluminum leads and an integrated 100-nm-thick Cu/Al aperture. Table 1 gives basic device parameters. The dominant cooling mechanism, which sets the detector time constant of ≈800 ns, is electron–phonon coupling in the Ti (electron outdiffusion is blocked by Andreev reflection in the superconducting Al leads). The TES is operated in negative electro-thermal feedback mode by wiring it in parallel with a small shunt resistor (see Table 1) and providing a current bias to the parallel combination [10]. Joule heating stabilizes the TES on its transition, and the operating resistance is about 2.3 Ω. The current through the TES is read out with a SQUID amplifier and room-temperature electronics from Magnicon [11], which are coupled to a fast (6 GHz) digitizing oscilloscope. Energy deposited in the voltage-biased TES results in a negative current pulse with an integrated charge that is proportional to the energy absorbed.

Table 1 Characteristics of the Ti TES with Al leads and an integrated 100-nm-thick Al/Cu thin-film aperture

Physical		**External**	
Width	10 μm	L_{total}	50 nH
Length	15 μm	R_{shunt}	200 mΩ
Thickness	15 nm	$R_{\text{parasitic}}$	5 mΩ
R_{Normal}	48.6 Ω	T_{bath}	100 mK
R_{Operate}	2.3 Ω	V_{Operate}	3.5 μV
T_{c}	345 mK	I_{bias}	18 μA

Henceforth, we refer to these pulses as 'events'. Event pulses are recorded, filtered, and fit to a model-pulse derived from the TES response to several thousand single blue photon events. The integral of the resulting best fit pulse is then scaled by the TES efficiency to give our best estimate of the incident energy.

The TES is protected by a thin-film aperture intended to absorb and diffuse energy deposited near, but not directly into the TES. The aperture is fabricated by evaporating a 100-nm-thick Cu/Al bi-layer on top of a thick $1-$ μm layer of insulating polymethylmethacrylate (PMMA) spun directly onto the wafer and then etching a window directly over the TES. The full fabrication process of the TES is detailed in the appendix, and Fig. 1a shows a side view of the layers. Figure 1c and b show optical and SEM images respectively.

We characterized our detector response with a pulsed blue (2.6 eV) laser, in the same manner as in Carter et al. [8]. By illuminating the TES with a pulsed source of low average photon number and making a histogram of the measured TES pulse-areas, one may calculate the TES energy resolution and efficiency by fitting the histogram with a Gaussian-broadened Poisson distribution.

3 Experimental Setup

The TES was mounted on the inner wall of a $5 \times 5 \times 5$ cm^3 helium-filled chamber, held at a temperature of 100 mK. The helium was pure ^{4}He (less than 1 part in 10^{12} ^{3}He) produced at Lancaster University using the heat-flush technique [12]. Excimers were created in the helium bath in two ways. The first method employed a ^{22}Na gamma-ray source external to the cryostat. Compton scattering in the helium produces electron recoils extending to hundreds of keV. These high-energy electrons lose their energy to the surrounding He atoms by exciting and ionizing He atoms, which upon electron–ion recombination produce a mixture of singlet and triplet excimers. The second method for excimer production was to apply a large negative voltage (~ -1.5 kV) to a sharp tungsten tip immersed in the He bath. Electrons emitted from the tip lose energy to the bath, producing atomic excitations, rotons, and quantized vortex rings. Both production methods were employed with consistent results. Here we report results from the ^{22}Na method, which allowed a cleaner timing selection (through the use of a coincidence trigger as explained below) and lower electronic readout noise.

When using the ^{22}Na source, some fraction of the gamma rays will Compton-scatter within the Si substrate rather than in the He. Such substrate energy depositions were

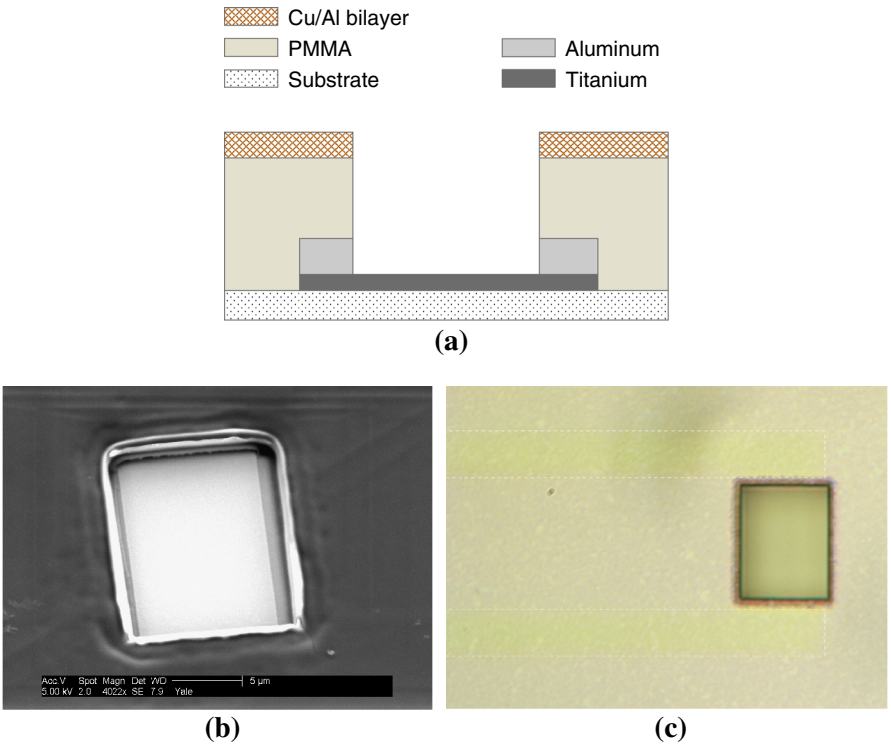

Fig. 1 **a** Cross-sectional diagram of TES configuration (not to scale, dimensions in Table 1). **b** SEM image of TES with aperture. **c** Optical image of TES with aperture. Leads are just visible extending to the left underneath the Cu/Al shield layer (outlined in *dashed white*) (Color figure online)

observed and excluded from the analysis using a pulse shape selection, which takes advantage of the relatively slow diffusion of phonons within the substrate, and their relatively weak coupling to the TES. Figure 2 shows two scatter plots of pulse height vs. pulse area for events measured under ^{22}Na irradiation. The events in Fig. 2a were recorded with the chamber empty of helium, and the events in Fig. 2b were recorded after condensing He. In both sets of data, a population corresponding to large pulse energies (10–1000 eV) and large pulse heights (30–1000 nA) was observed; this is the substrate absorption signal (the cutoff near 1000 nA is due to detector saturation). Random noise triggers are included as a blob in the lower left of each plot. In Fig. 2b, two populations of much faster (larger height-to-energy ratio), lower-energy pulses may be observed. The upper population (colored in blue) results from direct absorption of energy in the TES from either a singlet photon or a triplet quench. The lower population is due to events near the TES (i.e., the leads, the substrate below the TES) All of the following data analysis focuses solely on the 'direct hits' (blue), which are selected by windowing on events with time-constants that match the intrinsic TES time constant.

Each ^{22}Na decay produces two counter-propagating 511-keV gamma rays and a single 1.3-MeV gamma ray. Thus, by adding a standard NaI scintillator coupled to a

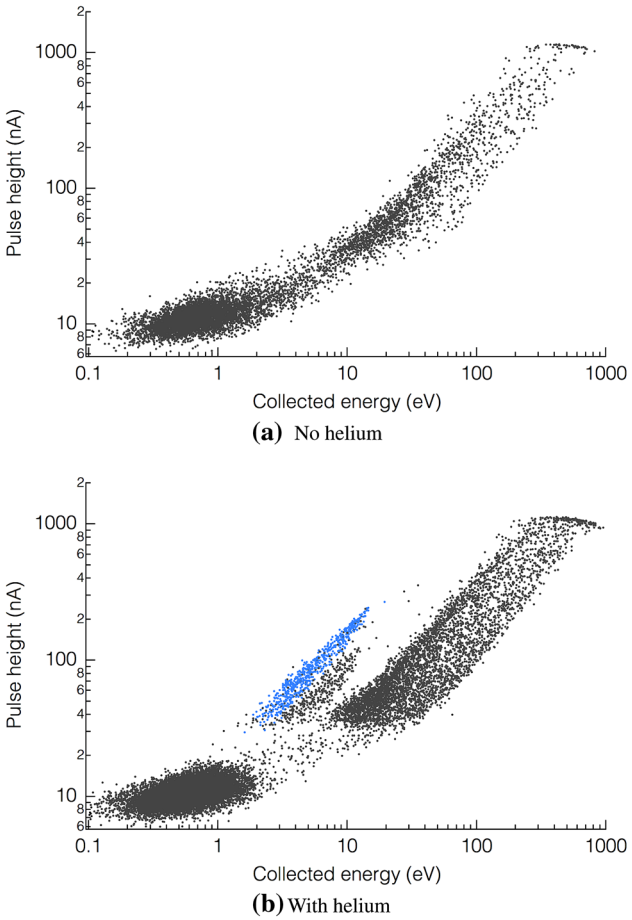

Fig. 2 **a** Pulse heights versus collected energy recorded with the TES while an empty chamber was subject to a ^{22}Na gamma-ray source. **b** The same, except in this case the chamber was filled with superfluid helium. *Blue points* correspond to direct excimer detection events in the TES (both singlet and triplet). The "extra" population located just below the *blue points*, but not present in (**a**), is due to energy deposited near the TES, but not directly in it (i.e., leads, substrate nearby) (Color figure online)

photo-multiplier tube (PMT) opposite the helium chamber, we may tag TES events coincident with a ^{22}Na decay. Figure 3a illustrates the geometry for this setup. Singlet decay photons are emitted promptly (ns scale) after the gamma-ray/electron recoil, whereas triplet excimers arrive at the TES delayed by a ballistic propagation time measured by Zmeev et al. [6] to be ∼2 m/s. These dramatically differing timescales imply that any TES event which is coincident (within 250 ns) with a PMT signal must arise from the collection of a prompt photon, or a triplet state excimer that was created within a distance of less than 12 μm from the TES. The chamber is big enough that this small population of triplets will contribute fewer than one out of every 50 detection events and may thus be neglected.

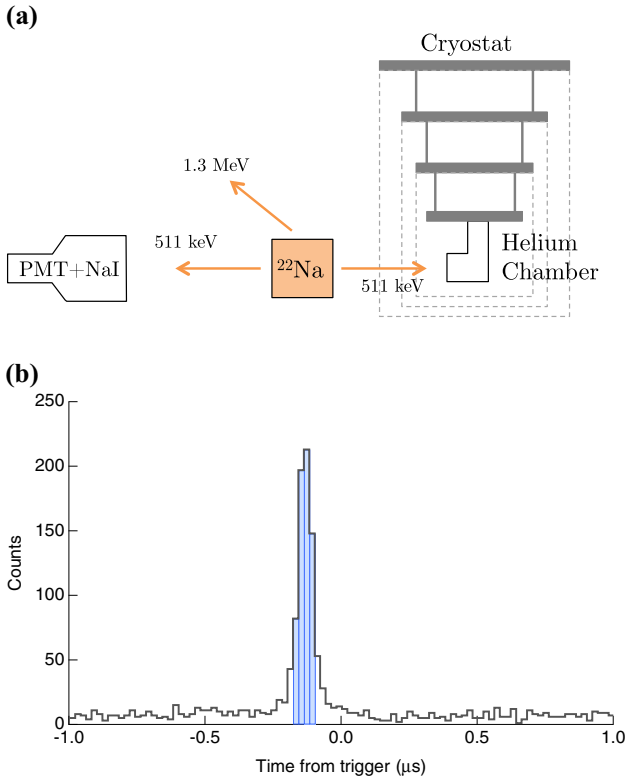

Fig. 3 **a** Experimental setup for coincidence measurements with a ^{22}Na source. The PMT + NaI detector and the helium chamber are aligned relative to the radiation source such that the solid angles of illumination are matched. Any 511-keV gamma ray that is incident on the chamber will also produce a 511-keV gamma ray that is incident on the PMT + NaI detector. **b** Histogram of the time difference between pulses detected in the PMT channel and pulses detected in the TES channel; substrate events have been removed. The shaded region is the cut used to make the red curve in Fig. 4 (Color figure online)

The PMT output is continuously monitored by the same oscilloscope that monitors the TES. Whenever a TES signal triggers the oscilloscope, it collects 5 μs of data before the trigger and 45 μs after the trigger. The rising edge of any pulses observed in the PMT channel is recorded as delay times relative to the trigger time at $t = 0$. Figure 3b shows a histogram of delay times between TES events (at $t = 0$) and PMT events. The large peak near zero delay is due to photon absorption events in the TES that were coincident with a gamma-ray detection in the PMT. The ≈100 ns offset from zero reflects the combined effects of cable-length delay and the placement of the TES trigger partway up the rising edge of the TES pulse.

4 Results

Figure 4 shows two energy spectra created by binning ∼13 000 single excimer detection events by the energy measured with the TES. The blue curve is a spectrum of all

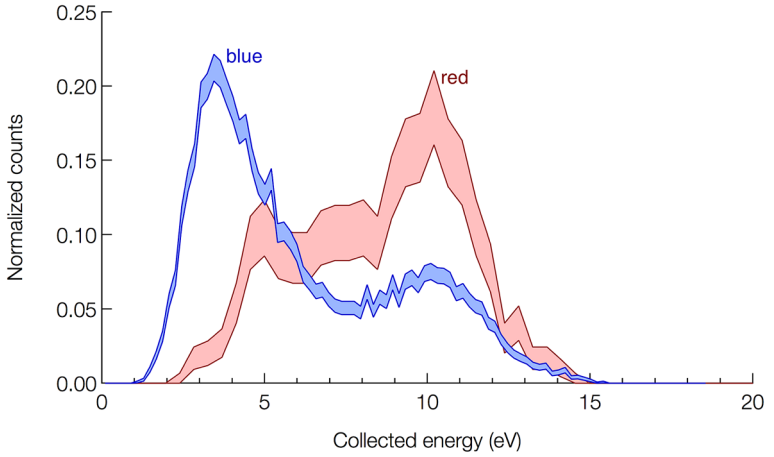

Fig. 4 *Red curve* Detected emission spectrum of singlet He_2^* decays (683 counts). *Blue curve* Total spectrum of all detected events (13 256 counts). *Shaded area between lines* indicates error, calculated as ± the square-root of the counts in each bin (Color figure online)

the TES events due to irradiation by the ^{22}Na source (the population of events colored blue in Fig. 2b). The red curve shows a spectrum consisting of only the coincident events (the events in the shaded region of the histogram in Fig. 3b), which must arise from detecting singlet photons (plus a 3% contribution from non-coincident events due to random coincidence). The shaded area indicates the error, calculated as the square-root of the number of counts in each bin. The two curves have been scaled such that their areas are each equal to unity. We hypothesize that the large peak in the blue curve near 3.5 eV arises mostly from the detection of triplet state excimer quenches on the TES surface, although it is clear that the photon-only signal (red curve) also has a small contribution in that energy range.

4.1 Discussion

4.1.1 Coincident Spectrum (Red Curve)

The primary feature of the helium scintillation spectrum as measured previously by Stockton et al. [13] is a peak centered at 15.5 eV with a full-width-half-maximum of about 3 eV. One would expect the red spectrum in Fig. 4 to look qualitatively similar, as it is due almost entirely to scintillation photons. Instead, the coincident spectrum peaks somewhat lower, near 10 eV, and shows a tail toward lower energies. It is possible that the detector response may not be linear from 2.65 eV (the calibration energy using blue photons) to this higher 15.5 eV range. We investigated TES linearity at low energy experimentally by comparing our 2.65-eV calibration with a separate 0.8-eV calibration; results were consistent with linearity in this range (an identical fraction of photon energy appeared in the TES electron system during the absorption of a single photon: 67 %). Calibration at higher photon energies was not performed as we did not have access to such a photon source.

In order to estimate the efficiency of our TES at higher energies, we calculated the energy lost during a photon absorption according to Kozorezov et al. [14]. When the detector absorbs a single photon, all of the energy is initially contained in a single excited photoelectron. This excited electron transfers its energy to the electron system, which arrives at a thermal distribution and then cools off through phonon scattering. This is a four-step process. Step 1: The initial photoelectron shares its energy with other electrons within a radius of about 20 pm via electron–electron interactions until the mean electron energy in the hot spot is about 800 meV, independent of initial energy (this is a material property of Ti). This process takes of order 100 fs. Step 2: The athermal electrons then shed phonons until the rate of phonon emission roughly matches the rate of phonon absorption, which happens at a mean energy per electron of about 4 meV for titanium and takes a time of order a few picoseconds. Step 3: The hot spot of electrons shares its energy with the rest of the system through electronic interactions and arrives at a thermal distribution within a few nanoseconds. Step 4: The thermal electrons cool through phonon scattering over a timescale of order 1 μs for our device. This characteristic time is shortened to about 700 ns in our experiment through electro-thermal feedback due to the voltage bias. During Step 2 of this process, a large amount of the initial photon energy is converted into athermal phonons. For a thin-film device (thinner than the athermal phonon mean-free-path), the chance of energy loss due to phonons escaping into the substrate is high. We have calculated that for our device this loss should be about 30 % of the initial energy, a value that is consistent with our experimentally determined device energy efficiency of 67 %. However, we find that this efficiency does not depend on initial photon energy (unless the initial photon energy is smaller than 800 meV in which case the energy loss will be less) and so can not explain the apparent nonlinear effect we observe at 15 eV.

There are at least three remaining possible additional channels for energy loss during a photon event. At the beginning of Step 4, the hot electrons have a mean energy of about 4 meV, which is roughly 20 times higher than the aluminum superconducting energy gap (Δ). The time for an electron to diffuse from the center of the TES to the edge ($\tau = L^2/D$, where L is the distance to the contact and D is the diffusion coefficient) is about 80 ns, which is of the same order as the time it takes the hot spot to settle into a thermal distribution below the Al energy gap. This allows for the possibility that some hot electrons could escape out the Al leads prior to thermalization. The energy lost in this process should be a linear function of the initial number of hot electrons present and so a linear function of photon energy. Our two-point calibration (0.8 eV and 2.6 eV) does not exhibit any significant efficiency variation and so we discount this loss mechanism.

The second energy loss channel is the photoelectric effect. At the beginning of Step 1, a photoelectron with energy greater than the Ti work function (4 eV) may simply escape the TES entirely. This can happen either immediately or after sharing some of its energy with the electron system. Mancini et al. [15] show that for thin films, the escape probability is proportional to $1/d$ where d is the film thickness. Studies of photoelectron yield for micron-thick Ti films give yields as large as 20 % [16], suggesting that a 100 % yield for a very thin film is not unreasonable. When a photoelectron escapes, it leaves a hole below the Fermi surface that is filled by an electron from the Fermi level, releasing the remainder of the energy into the TES

according to the four-step process above. Walker and Weissler [17] studied the energy spectrum of photoelectrons emitted from a gold film during illumination from a 14-eV source and found a large fraction of escaping photoelectrons with very low energies (∼3 eV) suggesting that they came from deep in the Fermi sea. If a similar process were occurring in our detector with 100 % conversion rate, it would explain the apparent drop in efficiency at 15 eV that we observe. Furthermore, Ti has wide bands near 2 and 5 eV below the Fermi surface and the low-energy tail from about 4–9 eV could be explained by a smaller population of photoelectrons ejected from these bands.

The third loss channel relies on the TES having surface oxidation. A 15-eV photon is large enough to remove an oxygen ion through a photon-assisted Auger process [18]. The characteristic energy of the ejected O^+ is about 4 eV, so for a 15-eV photon, 11 eV would be deposited in the TES. We expect the occurrence of this phenomenon to be quite low, but include it here for completeness.

Finally, we note that Cabrera et al. [19] characterized a thin-film tungsten TES at energies from near-IR up to 3.5 eV and found that while their device was linear up to 3 eV, it experienced an onset of decreased efficiency above 3 eV (see Fig. 4, inset, in their paper). This motivates further study of the energy loss of thin-film TES devices in the vacuum-ultraviolet energy range where photoelectric and Auger processes may be important.

4.1.2 Total Spectrum (Blue Curve)

The total spectrum (collected without regard to coincidence in the PMT channel) also shows the 10-eV peak that we attribute to absorption of singlet-state excimer decay photons; the coincidence trigger efficiency was low so we could not construct a data selection free from this prompt contribution. A second peak is observed near 3.5 eV, and we conclude that this peak represents the direct detection of triplet state excimers after a propagation delay.

Deexcitation of single He^* atoms through interaction with solid surfaces has been studied for the purpose of probing the electron density of states in a material's surface (metastable deexcitation spectroscopy). See, for example, Harada et al. [20], Bonini et al. [21] , or Trioni et al. [22]. He_2^* deexcitation (or quenching) at a surface is expected to proceed in a similar fashion. Figure 5 depicts the manner in which an excimer quenches at the surface through electron exchange, coupling a fraction of its 15.5-eV excitation energy into the TES surface. The process is as follows:

1. As the excimer comes within angstrom-scale distance of the TES surface, the excited electron resonantly tunnels into an empty state (at energy E_1) above the metal's Fermi level (E_F), leaving the excimer charged as He_2^{*+}. This electron at E_1 then scatters down to the Fermi energy, releasing an energy ($E_1 - E_F$) into the TES. For this 'resonant ionization' process to occur, the work function of the TES surface must be greater than $E_v - E_1$ where E_v is the vacuum energy. It should be noted that both the surface and He_2^* electron energies vary as a function of surface-He_2^* separation (excimer electron energies increase slightly as distance decreases).

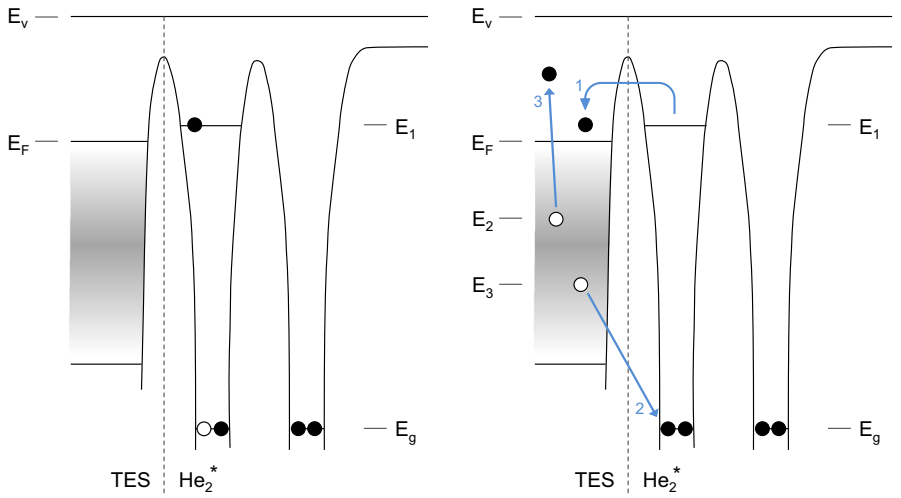

Fig. 5 **a** The triplet state excimer is to the *right of the dashed line* (one He atom in the ground state and one in an excited state) and the TES is to the *left of the dashed line*. The horizontal axis is distance, and the vertical axis is energy. E_v is the vacuum energy and E_F is the Fermi energy of the TES. E_g is the ground-state energy of the excimer. The gradient region depicts an arbitrary non-uniform density of states below the Fermi level in the TES. $E_1 - E_g$ is the excimer energy and is about 15 eV. E_1 is roughly 4 eV below E_v, but shifts upwards as the excimer approaches the TES surface. **b** The processes involved in the excimer quenching on the detector (*blue arrows*) is numbered in order of occurrence 1: the excited electron tunnels into a free state in the TES and relaxes to the Fermi surface. 2: An electron from the TES Fermi sea fills the empty ground state of the helium molecule, and the molecule splits into two atoms. 3: An Auger electron is promoted from within the TES Fermi sea and has energy $E_3 - E_g$. Finally, electrons relax from the Fermi surface to fill the two empty states in the TES (this is not pictured). Energies E_2 and E_3 are arbitrary as these two electrons may source from anywhere in the TES Fermi sea (Color figure online)

2. An electron from the metal surface then tunnels in the opposite direction, filling the vacancy in the ground state to neutralize the He_2^{*+}. The dimer separates.
3. An electron from within the Fermi sea gains the energy released in the previous step ($E_3 - E_g$) through an Auger process. This may be enough energy to cause the electron to escape the TES. This and the previous step are often termed 'Auger neutralization'.
4. Finally, electrons from the Fermi surface cascade down to fill the two holes left by the neutralizing electron and the Auger electron. These two energies are $E_F - E_3$ and $E_F - E_2$. If the Auger electron from the previous step remains within the TES, it will deposit the rest of its energy, $(E_3 - E_g) - (E_F - E_2)$, in the TES as it relaxes to the Fermi level.

In this process, $E_1 - E_F$ is always deposited in the TES. For a Ti TES, this energy is very nearly zero. The two electrons from steps 2 and 3 can come from any filled state in the TES, and so the density of states plays a large role in determining E_2 and E_3. There is also no reason why E_2 should be larger than E_3. This process effectively maps out the density of states near the Fermi level and is nearly the inverse of metastable deexcitation spectroscopy. In that process the Auger electron is collected when it

escapes from the surface, whereas in this case, the TES collects the energy that does not escape. Thus, the spectral shape will be heavily influenced by both the density of states near the Fermi surface of the TES and the detector's response to input energy.

This explanation relies on the efficient escape of Auger electrons from their origin in the outermost atomic layer of the TES. While there are no measurements of this escape probability specifically for He_2^* metastable deexcitation on Ti, there are a variety of measurements on other metals for the similar He^* deexcitation process. The Auger electron escape probability has been observed to range from ≈ 0.45 to > 0.90 depending on metal and surface treatment (generally higher for air-contaminated surfaces), consistent with our observations [23].

5 Conclusion

We have demonstrated the calorimetric detection of individual He_2^* excimers in two distinct channels with a TES immersed directly in superfluid helium. The short-lived singlet states are visible through their ≈ 15 eV scintillation photons, well above threshold of the device. The long-lived triplet states are also detectable through their few-eV energy deposition upon arrival at the TES surface. The two signals are distinguishable (in aggregate) by their spectral shapes.

The energy deposited during the interaction of the triplet excimer with the TES surface is expected to be highly dependent on the TES surface's electronic density of states. In our case, we posit that the oxidized Ti surface allowed the efficient transfer of a fraction of the excimer energy into the surface by taking advantage of bands located between 2 and 5 eV below the Fermi energy. In a future version of this experiment, this density of states could be engineered to generate a signal of higher efficiency or fidelity. The eventual application of these new excimer detection principles toward instrumenting a large volume with high excimer detection efficiency will depend on applying them to larger-area calorimeters (see Angloher et al. [24] or Pyle et al. [25]).

One promising application for our detector concept lies in studies of quantum turbulence. Given the large (96 nm) trapping diameter for He_2^* molecules on quantum turbulence vortices [7], high-efficiency detection of these excimers should enable sensitive monitoring of quantum turbulence density by measuring the He_2^* flux passing through a superfluid helium-filled volume. This technique would also allow for independent monitoring of the He_2^* production from sharp tungsten tips held at a high voltage and used to decorate quantum turbulence with He_2^* excimers.

Finally, we note that there is a considerable uncertainty as to the exact physics underlying the spectral shapes presented in Fig. 4. We have put forward a hypothesis that appeals to the surface electron density of states, the photoelectric effect, and Auger processes, but there is no detailed model. A full understanding is not possible within the limits of the current data, and a new set of experiments and devices will be required to obtain a detailed theoretical explanation of these promising first results.

Acknowledgments We would like to thank Prof. M. Devoret for the loan of a dilution refrigerator; J. Cushman for drafting expertise; C. Matulis for circuit-board design; Dr. L. Frunzio for fabrication advice; Prof. R. Schoelkopf and Prof. M. Hatridge for cryogenics expertise; Dr. E. Bernard, Dr. C. McKitterick, Dr. Z. Leghtas, and S. Touzard for helpful discussions; and the Gibbs Machine Shop for making experimental

hardware. Facilities use was supported by YINQE and NSF MRSEC DMR-1119826. We also acknowledge support from the National Science Foundation under NSF DMR-1007974 and the Engineering and Physical Sciences Research Council (UK) under grant EP/H04762X/1.

Appendix: Fabrication

The TES was fabricated on a bare (unoxidized) high-resistivity silicon wafer. All the metal depositions were accomplished using electron beam (E-beam) evaporation in a commercial evaporator from Plasma Systems. The patterning was done using electron beam lithography in a Raith EBPG 5000+ system.

1. *Alignment marks* The wafer is cleaned, and a bilayer of polymethylmethacrylate (PMMA) E-beam resist is applied. A pattern of $20 \times 20\ \mu m^2$ squares are written via E-beam, and then 400 nm of Cu is evaporated and lifted-off to define the alignment marks. These marks are used to precisely position the etch window over the region destined to become the TES.
2. *Ti/Al bilayer* A bilayer of PMMA is applied. The outline of the detectors, wiring, and absorbers is written via E-beam. Then a bilayer of 15 nm of Ti and 300 nm of Al is evaporated and lifted-off.
3. *Al etch* A single layer of PMMA is applied. Windows are opened in the resist via E-beam lithography directly over the areas that are to become the TES. The exposed Al is then etched down to the Ti, defining the detectors (Ti is a natural etch stop for the etchant used).
4. *Aperture* The device is coated with a 1 μm thick layer of PMMA. Then a bilayer of 50 nm of Cu and 50 nm of Al is evaporated. An additional single layer of PMMA is applied, and a window is opened up over the TES. The Al and Cu are both etched away, leaving the 1 μm layer of PMMA. This layer is then developed away, as it received a weak dose of E-beam current during the earlier E-beam write.

References

1. D.N. McKinsey, C.R. Brome, J.S. Butterworth, S. Dzhosyuk, P.R. Huffman, C. Mattoni, J.M. Doyle, R. Golub, K. Habicht, Radiative decay of the metastable $He_2(a^3\Sigma_u^+)$ molecule in liquid helium. Phys. Rev. A **59**(1), 200–204 (1999). doi:10.1103/PhysRevA.59.200
2. W. Guo, M. La Mantia, D.P. Lathrop, S.W. Van Sciver, Visualization of two-fluid flows of superfluid helium-4. Proc. Natl. Acad. Sci., **111**(Supplement_1): 4653–4658 (March 2014). doi:10.1073/pnas.1312546111. http://www.pubmedcentral.nih.gov/articlerender.fcgi?artid=3970863&tool=pmcentrez&rendertype=abstract. http://www.pnas.org/cgi/doi/10.1073/pnas.1312546111
3. W. Guo, D.N. McKinsey, Concept for a dark matter detector using liquid helium-4. Phys. Rev. D Part. Fields Gravit. Cosmol. **87**(11), 115001 (2013). doi:10.1103/PhysRevD.87.115001
4. W.G. Rellergert, S.B. Cahn, A. Garvan, J.C. Hanson, W.H. Lippincott, J.A. Nikkel, D.N. McKinsey, Detection and imaging of He_2 molecules in superfluid helium. Phys. Rev. Lett. **100**, 025301 (2008). doi:10.1103/PhysRevLett.100.025301
5. W. Guo, J.D. Wright, S.B. Cahn, J.A. Nikkel, D.N. McKinsey, Metastable helium molecules as tracers in superfluid ^{4}He. Phys. Rev. Lett. **102**, 235301 (2009). doi:10.1103/PhysRevLett.102.235301

6. D.E. Zmeev, F. Pakpour, P.M. Walmsley, A.I. Golov, P.V.E. McClintock, S.N. Fisher, W. Guo, D.N. McKinsey, G.G. Ihas, W.F. Vinen, Observation of crossover from ballistic to diffusion regime for excimer molecules in superfluid ^{4}He. J. Low Temp. Phys. **171**(3–4), 207–213 (2013a). doi:10.1007/s10909-012-0720-6
7. D.E. Zmeev, F. Pakpour, P.M. Walmsley, A.I. Golov, W. Guo, D.N. McKinsey, G.G. Ihas, P.V.E. McClintock, S.N. Fisher, W.F. Vinen, Excimers He_2^* as tracers of quantum turbulence in ^{4}He in the T = 0 limit. Phys. Rev. Lett. **110**(17), 175303 (2013b). doi:10.1103/PhysRevLett.110.175303
8. F.W. Carter, S.A. Hertel, M.J. Rooks, D.N. McKinsey, D.E. Prober, Toward the in situ detection of individual He_2^* excimers using a Ti TES in superfluid helium. IEEE Trans. Appl. Supercond., **25**(3): 1–7 (June 2014). doi:10.1109/TASC.2014.2372673. http://ieeexplore.ieee.org/lpdocs/epic03/wrapper.htm?arnumber=6963369
9. F. W. Carter. A transition-edge-sensor-based instrument for the measurement of individual He_2^* excimers in a superfluid 4He bath at 100 mK. PhD thesis, Yale University, 2015
10. K.D. Irwin, An application of electrothermal feedback for high resolution cryogenic particle detection. Appl. Phys. Lett., **66**(15): 1998 (1995). doi:10.1063/1.113674. http://scitation.aip.org/content/aip/journal/apl/66/15/10.1063/1.113674
11. D. Drung, C. Aßmann, J. Beyer, A. Kirste, M. Peters, F. Ruede, Th. Schurig, Highly sensitive and easy-to-use SQUID sensors. IEEE Trans. Appl. Supercond., **17**(2): 699–704 (June 2007). doi:10.1109/TASC.2007.897403. http://ieeexplore.ieee.org/lpdocs/epic03/wrapper.htm?arnumber=4277368
12. P.V.E McClintock, An apparatus for preparing isotopically pure ^{4}He. Cryogenics, **18**(4): 201–208 (Apr 1978). doi:10.1016/0011-2275(78)90002-4. http://linkinghub.elsevier.com/retrieve/pii/0011227578900024
13. M. Stockton, J.W. Keto, W.A. Fitzsimmons, Ultraviolet emission spectrum of electron-bombarded superfluid helium. Phys. Rev. Lett., **24**(12): 654–657 (March 1970). doi:10.1103/PhysRevLett.24.654. http://journals.aps.org/prl/abstract/10.1103/PhysRevLett.24.654. http://link.aps.org/doi/10.1103/PhysRevLett.24.654
14. A.G. Kozorezov, C.J. Lambert, S.R. Bandler, M.A. Balvin, S.E. Busch, P.N. Nagler, J.-P. Porst, S.J. Smith, T.R. Stevenson, J.E. Sadleir, Athermal energy loss from X-rays deposited in thin superconducting films on solid substrates. Phys. Rev. B **87**, 104504 (2013). doi:10.1103/PhysRevB.87.104504
15. N.A. Mancini, G. Giaquinta, A. Pennisi, Quantum size effects and optical properties of very thin films. J. Opt. Soc. Am., **71**(4): 383 (Apr 1981). doi:10.1364/JOSA.71.000383. http://stacks.iop.org/1402-4896/23/i=5A/a=012?key=crossref.cf8148e287c1c3351972f417865ae9fb. https://www.osapublishing.org/abstract.cfm?URI=josa-71-4-383
16. R.B. Cairns, J.A.R. Samson, Metal photocathodes as secondary standards for absolute intensity measurements in the vacuum ultraviolet **56**(11), 1568–1573 (1966). doi:10.1364/JOSA.56.001568
17. W.C. Walker, G.L. Weissler, Vacuum ultraviolet optical and photoelectric effects in solids. J. Quant. Spectrosc. Radiat. Transf. **2**(4), 613–620 (1962). doi:10.1016/0022-4073(62)90047-X
18. D.M. Hanson, R. Stockbauer, T.E. Madey, Photon-stimulated desorption and other spectroscopic studies of the interaction of oxygen with a titanium (001) surface. Phys. Rev. B **24**(10), 5513–5521 (1981). doi:10.1103/PhysRevB.24.5513
19. B. Cabrera, R.M. Clarke, P. Colling, A.J. Miller, S. Nam, R.W. Romani, Detection of single infrared, optical, and ultraviolet photons using superconducting transition edge sensors. Appl. Phys. Lett., **73**(6): 735 (1998). doi:10.1063/1.121984. http://scitation.aip.org/content/aip/journal/apl/73/6/10.1063/1.121984
20. Y. Harada, S. Masuda, H. Ozaki, Electron spectroscopy using metastable atoms as probes for solid surfaces. Chem. Rev., **97**(6): 1897–1952 (1997). doi:10.1021/cr940315v. http://www.ncbi.nlm.nih.gov/pubmed/11848894
21. N. Bonini, G.P. Brivio, M.I. Trioni, Theory of metastable deexcitation spectroscopy on simple metals. Phys. Rev. B **68**, 035408 (2003). doi:10.1103/PhysRevB.68.035408
22. M.I. Trioni, G. Butti, N. Bonini, G.P. Brivio, Metastable helium spectroscopy on simple metals: comparison between low and high work function substrates. Surf. Sci., **587**(1–2): 121–127 (August 2005). doi:10.1016/j.susc.2005.04.040. http://linkinghub.elsevier.com/retrieve/pii/S0039602805004474
23. F.B. Dunning, *Atomic, Molecular, and Optical Physics: Atoms and Molecules*, vol. 29B (Academic Press, London, 1996)
24. G. Angloher, C. Bucci, P. Christ, C. Cozzini, F. von Feilitzsch, D. Hauff, S. Henry, T. Jagemann, J. Jochum, H. Kraus, B. Majorovits, J. Ninkovic, F. Petricca, W. Potzel, F. Pröbst, Y. Ramachers, M. Razeti, W. Rau, W. Seidel, M. Stark, L. Stodolsky, A.J.B. Tolhurst, W. Westphal, H. Wulandari,

Limits on WIMP dark matter using scintillating $CaWO_4$ cryogenic detectors with active background suppression. Astropart. Phys. **23**(3), 325–339 (2005). doi:10.1016/j.astropartphys.2005.01.006
25. M. Pyle, E. Feliciano-Figueroa, B. Sadoulet, Optimized designs for very low temperature massive calorimeters (2015). arXiv:1503.01200v2